AerospaceEurope Conference2020
BORDEAUX, FRANCE | 25 - 28 FEBRUARY 2020

TURBULENCE PREDICTION FOR AIRCRAFT BY MEANS OF HIGH-DYNAMIC DIFFERENTIAL PRESSURE MEASUREMENTS

Andras Galffy [(1) (2)], Johannes Schlarp[(2)], Daniel Frank[(2)], Robert Mühlbacher[(3)], Georg Schitter[(2)]

(1) Corresponding author, Email: galffy@acin.tuwien.ac.at
(2) Automation and Control Institute, TU Wien, Gusshausstrasse 27-29/E376, 1040 Vienna, AUSTRIA
(3) Turbulence Solutions, Wollzeile 1-3/3.2, 1010 Vienna, AUSTRIA

KEYWORDS:
atmospheric turbulence, disturbance prediction, turbulence suppression, gust load alleviation

ABSTRACT:

This paper focuses on the prediction of disturbance effects of the vertical acceleration of an aircraft in atmospheric turbulence. To this end, 5-hole probes with high-dynamic differential pressure sensors are installed in front of a fixed-wing unmanned aircraft system (UAS) to measure the local airspeed and angle of attack of the airflow. Test flights are performed in moderate and severe turbulence to assess the anticipating character and the accuracy of the predicted acceleration. Thereby, depending on the flown airspeed, anticipation times up to 0.1s are observed. The prediction accuracy is assessed to be 93.65% for moderate turbulence and 87.78% for severe turbulence, where vertical acceleration disturbances higher than 30m/s^2 are measured.

1. INTRODUCTION

While challenges for flight operations in low visibility and icing conditions are largely overcome, atmospheric turbulence still causes injuries, delays and major waste of resources, such as CO2 emissions and excessive fuel consumption [1]. Suppressing atmospheric turbulence in flight carries the potential to reduce CO2 emissions, fuel consumption and flight time by up to 10% for commercial flights [2], [3]. These potentials become even more relevant, as atmospheric turbulence is predicted to increase in response to climate change [4].

In this context, this paper investigates on the turbulence prediction task, c.f., Figure 1, which can be seen as a subtask of the turbulence suppression objective, also known as gust load alleviation [5]. The accurate prediction of disturbance effects subsequently enables the rejection of the disturbances by feedforward deflections of flight control surfaces of an aircraft [6].

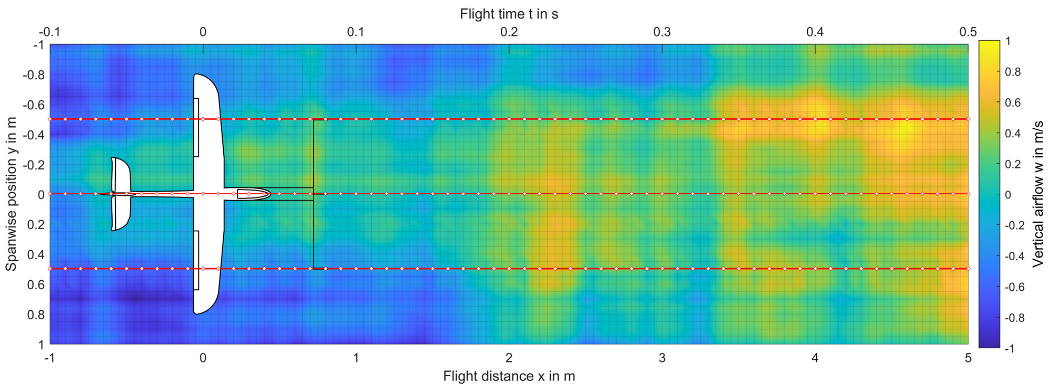

Figure 1: Unmanned aircraft flying in atmospheric turbulence. The vertical movement of the air is presented according to the colorbar on the right side (yellow for rising air, blue for sinking air). High-dynamic differential pressure sensors in front of the wings provide anticipating measurements of the turbulence field to predict disturbance effects. The three red lines indicate the lateral position of the probes, where measurements are taken at the positions of the white diamonds.

Atmospheric turbulence can be modelled making use of spatial power spectral densities (PSD). Examples are the von Kármán [7] and the Dryden [8] wind turbulence field model. Prior approaches to predict turbulence effects include wind LIDAR measurements [9], both for a statistical analysis of the far field to warn the flight crew [10], as well as for prediction of the near field in front of the aircraft for actuation of the flight control surfaces [11]. Other approaches include the use of pressure sensors [12] to counteract turbulence effects in wind tunnel tests. [12] also gives an overview of various sensor principles, both anticipating, such as differential pressure sensors [13] and strain gauges [14], as well as reactive measurements, e.g., inertial measurements used for acceleration control [15]. The disadvantage of reactive measurements is that rejection efforts can only be started upon measuring the first negative effects of the disturbance. Thus, only by including anticipating measurements, a theoretically perfect cancellation of disturbances is possible [16]. In contrast to simulative studies of aircraft models like [17] and wind tunnel tests like [18], literature is lacking research including actual test flight results.
The contribution of this paper is the presentation of actual test flight data measured with a UAS test platform for different turbulence intensities. The data is analyzed in the time domain, frequency domain, as well as for the statistical distribution. Section 2 presents an approach to model and analyse turbulence based on spectral characteristics. Section 3 describes the UAS testbed, which allows for anticipating measurements of the airflow in front of the wings. Section 4 states the calculations to transform measured wind quantities into predicted acceleration values. Finally, Section 5 presents the test flight data, which is assessed regarding the turbulence prediction task.

2. TURBULENCE MODELLING

For the spatial and temporal analysis of a wind field, which is traversed by an aircraft in atmospheric turbulence, spectral modelling is pursued. According to the Dryden wind turbulence model [8], the PSD of the vertical turbulence component *w* can be characterized by

$$\Psi_w(\Omega) = \sigma_w^2 \frac{2L_w}{\pi} \frac{1+12(L_w\Omega)^2}{(1+4(L_w\Omega)^2)^2}, \qquad (1)$$

with the spatial frequency Ω, the turbulence intensity σ_w, and the turbulence scale length L_w. To generate a representative turbulence field with a PSD according to (1) a suitable transfer function

$$G_w(s) = \sigma_w \sqrt{\frac{2L_w}{\pi} \frac{1+\sqrt{12}L_w s}{(1+2L_w s)^2}} \qquad (2)$$

can be found, which satisfies

$$\Psi_w(\Omega) = |G_w(j\Omega)|^2. \qquad (3)$$

Thus, by filtering 2-dimensional, unit-variance, band-limited white noise by (2) representative turbulence fields $w(x,y)$ can be generated, where x is the longitudinal coordinate in flight direction and y is the lateral, spanwise coordinate. In Fig. 1 an exemplary field with scale length $L_w = 3$m is shown, which is the scale length that is observed during test flights with the fixed-wing UAS. In the following, the different effects of spatial variations in x-direction and y-direction of such turbulence field shall be examined.
Spatial variations in x-direction are transformed into time variations as the aircraft flies through the turbulence field. Based on the airspeed V_a the relation of temporal frequency ω and spatial frequency Ω can be calculated as

$$\omega = V_a\Omega. \qquad (4)$$

In consequence, neglecting time change of the turbulence field itself, i.e. assuming a frozen turbulence model [19], a spatial PSD $\Psi_w(\Omega)$ can be transformed into a temporal PSD $\Phi_w(\omega)$ by

$$\Phi_w(\omega) = \frac{\Psi_w\left(\frac{\omega}{V_a}\right)}{V_a}. \qquad (5)$$

This implies that Φ_w gets broader and smaller for higher airspeeds V_a. For $L_w = 3$m and $\sigma_w = 1\frac{m}{s^2}$, Fig. 2 shows $\Psi_w(\Omega)$, $|G_w(j\Omega)|^2$, as well as $\Phi_w(\omega)$ for 3 different airspeeds $V_a = 10\frac{m}{s}, 30\frac{m}{s}, 100\frac{m}{s}$. It can be noticed that, the faster the aircraft is flying, the stronger the influence of higher temporal frequencies becomes.

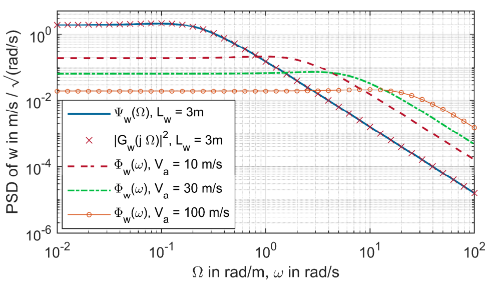

Figure 2: Spatial PSD $\Psi_w(\Omega)$, transfer function $|G_w(j\Omega)|^2$ and temporal PSD $\Phi_w(\omega)$ for three different airspeeds.

Spatial variations in y-direction, i.e., spanwise variations, determine to which extent various flight quantities, such as vertical acceleration, pitch moment, roll moment, wing bending and higher-order structural dynamics are affected. As an example, symmetric spanwise variations do not cause roll moments as the effects on the left and right wing cancel out.

To account for spanwise variations of the turbulence field, a representation of $w(y) = w(\cdot, y)$ by orthonormal polynomial functions is proposed. For this purpose, an inner product of two spanwise distributions $x_1(y)$ and $x_2(y)$ can be defined as

$$\langle x_1, x_2 \rangle = \frac{1}{b} \int_{-\frac{b}{2}}^{\frac{b}{2}} x_1(y) x_2(y) dy, \quad (6)$$

with the span b, and the according induced norm

$$\|x_1\| = \sqrt{\langle x_1, x_1 \rangle}. \quad (7)$$

Therewith, orthonormal polynomial basis functions can be defined by recursively applying the law

$$p_i(y) = \frac{\left(y^i - \sum_{j=0}^{i-1} \langle y^i, p_j(y) \rangle \, p_j(y)\right)}{\left\|\left(y^i - \sum_{j=0}^{i-1} \langle y^i, p_j(y) \rangle \, p_j(y)\right)\right\|} \quad (8)$$

for $i = 0, \dots, \infty$ to fulfil the relations

$$\langle p_i, p_j \rangle = \begin{cases} 1, i = j \\ 0, i \neq j \end{cases}. \quad (9)$$

An arbitrary spanwise wind distribution $w(y)$ can then be represented by a coefficient vector $\boldsymbol{\zeta} = [\zeta_0 \; \zeta_1 \; \zeta_2 \; \cdots]$ as

$$w(y) = \sum_{i=0}^{\infty} w_i(y) = \sum_{i=0}^{\infty} \zeta_i p_i(y), \quad (10)$$

where the coefficients can be calculated as

$$\zeta_i = \langle w, p_i \rangle. \quad (11)$$

Figure 3 shows the first three even basis polynomials p_0, p_2, and p_4, as well as the first three uneven basis polynomials p_1, p_3, and p_5 for b=1.6m. Additionally, an exemplary distribution $w_{0,5}$ acting on an aircraft is illustrated with $\boldsymbol{\zeta} = [1 \;\; 0.5 \;\; \text{-}1 \;\; \text{-}0.3 \;\; 0.2 \;\; \text{-}0.2 \;\; 0 \;\; 0 \;\; \cdots]$.

To quantify the variation of a spanwise wind distribution $w(y)$, the rooted mean square (RMS) value with (9) and (10) can be determined as

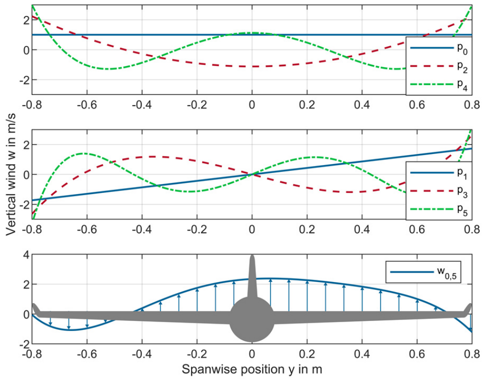

Figure 3: Even polynomials p_0, p_2, and p_4, odd polynomials p_1, p_3, and p_5, and distribution $w_{0,5}$.

$$RMS(w) = \|w\| = \sqrt{\langle w, w \rangle} = \sqrt{\sum_{i=0}^{\infty} \zeta_i^2} = \|\boldsymbol{\zeta}\|_2 \,, \quad (12)$$

where $\|\cdot\|_2$ denotes the Euclidean norm. Thus, the RMS value of the coefficient vector $\boldsymbol{\zeta}$, i.e., $\mathrm{RMS}(\boldsymbol{\zeta}) = \|\boldsymbol{\zeta}\|_2$, also represents the RMS value of w, where ζ_i is the contribution of the i-th component $w_i = \zeta_i p_i$. Assessing the statistical relevance of the i-th component, the ratio of the turbulence scale length L_w and the span b of the aircraft is decisive for the expected value $E(\zeta_i^2)$. In this regard, Figure 4 shows $\sqrt{E(\zeta_i^2)}$ of the first eight coefficients $\zeta_0, \zeta_1, \cdots, \zeta_8$ for different values of $\frac{L_w}{b} = 0.1, \; 1, 10$ to be able to assess the expected contribution of the i-th component w_i to $\mathrm{RMS}(w)$.

For $\frac{L_w}{b} = 10$ the scale length of the turbulence field is significantly higher than the span, i.e., mainly low frequent spatial variations occur. This relates to

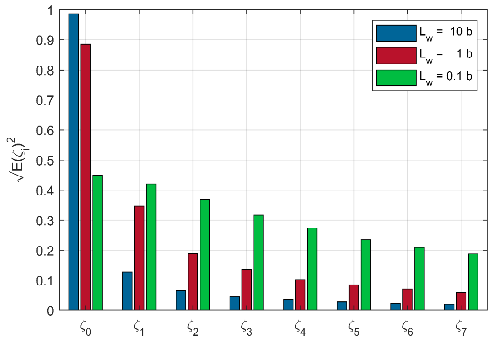

Figure 4: Expected value $\sqrt{E(\zeta_i^2)}$ of the first eight coefficients $\zeta_0, \zeta_1, \cdots, \zeta_8$ depending on $\frac{L_w}{b}$.

higher order coefficients ζ_i, $i > 2$, being of subordinate importance. For $\frac{L_w}{b} = 0.1$ the scale length of the turbulence field is significantly lower than the span, i.e., also higher order coefficients need to be included to properly represent the turbulence field.
These considerations need to be taken into account, when discrete measurements shall be performed for reconstruction of the turbulence field. If for example a single sensor is placed at the center of the aircraft, i.e., at $y = 0$, the measured vertical wind according to (10) is

$$w_c = \zeta_0 p_0(0) + \zeta_2 p_2(0) + \zeta_4 p_4(0) + \cdots, \tag{13}$$

as $p_i(0) = 0$ for $i = 1, 3, 5, \cdots$. If now w_c is used as estimated 0-th order coefficient $\hat{\zeta}_0 = w_c$, i.e., the center measurement is assumed to be valid for the whole span, spatial aliasing occurs leading to the relative error

$$\frac{\hat{\zeta}_0 - \zeta_0}{\zeta_0} = \frac{\zeta_2 p_2(0) + \zeta_4 p_4(0) + \cdots}{\zeta_0}, \tag{14}$$

as higher order coefficients are projected into $\hat{\zeta}_0$.

3. TEST FLIGHT SET-UP

To assess the suitability of differential pressure sensors to predict effects of atmospheric turbulence on the flight dynamics of an aircraft, a fixed-wing UAS test platform is constructed to measure the wind field in front of the aircraft, c.f., Figure 5. The UAS is based on the unmanned aircraft Volantex Ranger 1600 with a span of b=1.6m. At a distance $d_{x,CG} = \frac{b}{2} = 0.8\mathrm{m}$ in front of the aircraft's center of gravity (CG) airflow measurements are conducted at three different spanwise positions $y_L = -d_{y,CG} =$ -0.5m, y_C= 0m, $y_R = d_{y,CG} = 0.5\mathrm{m}$. With three independent measurements, the first three coefficients ζ_0, ζ_1, ζ_2 shall be determined, where ζ_1 is not used in this paper, however, will be used for future research on lateral dynamics. It may be noticed, that the third measurement is either way beneficial for determining ζ_2, as for two measurements only, parts of ζ_0 or ζ_1 would be projected into $\hat{\zeta}_2$, analogously to (14).
The airflow measurements are conducted by means of three individual 5-hole probes with a geometry as shown in Figure 6. The probes are 3D printed making use of resin-based stereolithography (SLA), which allows for fine resolutions as low as 47µm laterally and 20µm vertically. The pressure port p_1 is used to determine the local airspeed V_a, while pressure ports p_2 and p_3 are used to determine the local angle of attack (AOA) α of the respective probe. The pressure ports p_4 and p_5 could be used to determine the sideslip angle, however, are not connected and sealed rearwards, as lateral dynamics are not in the focus of the current investigations and the number of addressable sensors is limited. The static pressure p_s is taken from the fuselage and provided to the sensors in front of the aircraft by means of one common static pressure line.

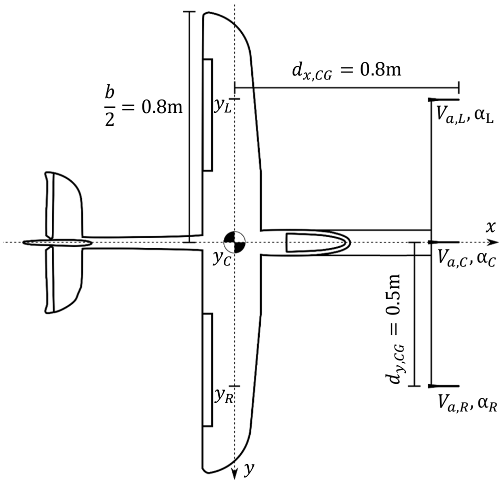

Figure 5: UAS test platform equipped with an air data boom with three 5-hole probes in front of the wings.

The difference of p_1 and static pressure p_s is measured as

$$\Delta p_{V_a} = p_1 - p_s \approx q = \frac{\rho}{2} V_a^2, \tag{15}$$

with the dynamic pressure q and the air density ρ to determine the airspeed according to

$$V_a \approx \sqrt{\frac{2\Delta p_{V_a}}{\rho}}. \tag{16}$$

The difference of p_2 and p_3 is measured as

$$\Delta p_\alpha = p_2 - p_3 \approx c_{p,\alpha} \alpha q, \tag{17}$$

with a constant coefficient $c_{p,\alpha}$ to determine the AOA according to

$$\alpha = \frac{\Delta p_\alpha}{c_{p,\alpha}\, q} \approx \frac{1}{c_{p,\alpha}} \frac{\Delta p_\alpha}{\Delta p_{V_a}}. \tag{18}$$

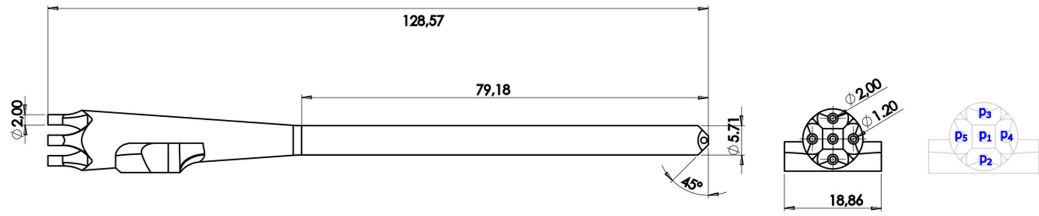

Figure 6: Geometry of the 5-hole probes to measure the airflow in front of the aircraft in mm. The probes are 3D printed by resin-based stereolithography. Pressure port p_1 is used for airspeed estimation, pressure ports p_2 and p_3 are used for angle of attack estimation. Pressure ports p_4 and p_5 are not connected and sealed rearwards.

Additionally, correction factors are implemented to correct quadratic measurement errors at higher AOA values according to [20]. The thereby achieved RMS measuring errors shown in [20] are 0.19m/s for V_a and 24mrad for α for a measuring range of 0m/s to 28m/s and -400mrad to 400mrad, respectively.

To measure Δp_{V_a} and Δp_α two individual differential pressure sensors (Sensirion SDP33) are used for each probe, thus, six sensors in total. As the ambient offset pressure of approximately 1bar = 10^5Pa is several orders of magnitude higher than the aerodynamic pressure changes in the order of q=100Pa, measuring differential pressures instead of subtracting absolute pressure measurements is pursued for improved accuracy. The measuring range of the differential pressure sensors of 1500Pa still allows airspeeds V_a up to 50m/s.

From the three airspeed measurements $V_{a,L}$, $V_{a,C}$, and $V_{a,R}$, c.f., Figure 5, the mean airspeed

$$V_a = \frac{1}{3}\left(V_{a,L} + V_{a,C} + V_{a,R}\right) \tag{19}$$

is determined, which is subsequently used as airspeed V_a.

As the probes are positioned $d_{x,CG}$ in front of the CG and the left and right probe are positioned $d_{y,CG}$ to the side of the CG, c.f., Figure 5, the roll rate ω_x and pitch rate ω_y cause local perpendicular airflow, which can be corrected by

$$\begin{aligned} \alpha_{L,CG} &= \alpha_L + \frac{d_{y,CG}\omega_y}{V_a} + \frac{d_{x,CG}\omega_x}{V_a}, \\ \alpha_{C,CG} &= \alpha_L + \frac{d_{y,CG}\omega_y}{V_a}, \\ \alpha_{R,CG} &= \alpha_L + \frac{d_{y,CG}\omega_y}{V_a} - \frac{d_{x,CG}\omega_x}{V_a}. \end{aligned} \tag{20}$$

Finally, for each of the considered AOA α_χ the corresponding local vertical wind w_χ can be calculated as

$$w_\chi = \alpha_\chi V_a. \tag{21}$$

Figure 7 shows the UAS before take-off, where the tubing from the 5-hole probes to the SDP33 sensors, which are placed at the center of the air data boom, can be seen. Furthermore, a mast is used together with cables to suppress vertical and torsional motions of the air data boom relatively to the fuselage by pretensioning. The battery is placed on the empennage to balance the CG, as the air data boom shifts the CG forward, which otherwise would lead to reduced maneuverability.

Figure 7: UAS testbed with air data boom equipped with three 5-hole probes, which are connected to high-dynamic differential pressure sensors.

The flight controller Pixhawk4 with customized firmware of the flight stack PX4 is positioned inside the fuselage close to the CG. The vertical acceleration a_z is measured by the on-board inertial measurement units. The cycle rate of the custom flight code is 500Hz, which is much higher than the investigated frequencies, allowing for quasi-continuous time considerations.

4. TURBULENCE PREDICTION

In this section the prediction of disturbances of the vertical acceleration a_z of an aircraft flying through atmospheric turbulence based on airflow measurements is discussed. The term prediction is

Aircraft	b	V_a	$T_b = b/V_a$
UAS	1.6m	10m/s	0.160s
MC-30	6.9m	45m/s	0.153s
PC-12	16.2m	100m/s	0.162s
A320	35.8m	200m/s	0.179s

Table 1: Comparison of span b, typical airspeed V_a, and ratio $T_b = b/V$ for four differently sized aircraft.

used in the sense, that by means of differential pressure measurements in front of the wing, c.f., Section 3, it is possible to calculate predicted values $\hat{a}_z$ with an anticipation time T_{ant} before a_z is expected to show these values, i.e.,

$$a_z(t) \approx \hat{a}_z(t - T_{ant}). \tag{22}$$

The predicted vertical acceleration $\hat{a}_z$ is calculated with the objective to minimize the prediction error

$$e_{a_z}(t) = a_z(t) - \hat{a}_z(t - T_{ant}). \tag{23}$$

For a frozen turbulence field and assuming that the airspeed V_a stays approximately constant during the comparatively short anticipation time T_{ant}, with the anticipation distance d_{ant} the anticipation time can be calculated as

$$T_{ant}(t) = \frac{d_{ant}}{V_a(t)}. \tag{24}$$

Considering examples of common aircraft types of different sizes, it is notable that the aircraft's airspeed increases approximately in the same order as the aircraft size. To this end, Table 1 lists the span b and typical airspeed V_a for the UAS of this paper, the ultra-light one-seater Colomban Luciole MC-30, the turbo-prop aircraft Pilatus PC-12, and the airliner Airbus A320. For all these types the ratio $T_b = b/V_a$ shows values in the order of 0.16s. This means that if anticipating measurements are performed at a half-span distance in front of the wings, i.e., $d_{ant} = \frac{b}{2}$, an anticipation time in the order of $T_{ant} = T_b = 0.08$s can be achieved.
To calculate $\hat{a}_z$ out of α and V_a measurements a simple lift force model [21] can be written as

$$L = (c_{L0} + c_{L\alpha}\alpha)\frac{\rho}{2}V_a^2\, S, \tag{25}$$

with air density ρ and wing area S, where lifting effects of turn rates and flight surface deflections are neglected. With the aircraft mass m the corresponding vertical acceleration a_z results as

$$a_z = \frac{L}{m} = \frac{\rho S}{2\,m}(c_{L0} + c_{L\alpha}\alpha)V_a^2. \tag{26}$$

With $c_{z0} = \frac{\rho S}{2\,m}c_{L0}$, $c_{z\alpha} = \frac{\rho S}{2\,m}c_{L\alpha}$ and $w = \alpha V_a$ a more concise form is found as

$$a_z = c_{z0}V_a^2 + c_{z\alpha}wV_a. \tag{27}$$

Thus, variations of the vertical wind w have direct effect on the vertical acceleration of the aircraft with the amplification factor $c_{z\alpha}V_a$. To take into account spanwise lift distributions, the basic model (27) can be extended by calculating the inner product $\langle c_{z\alpha}(y), w(y)\rangle$ instead of the scalar multiplication $c_{z\alpha}w$ resulting in the model

$$a_z = c_{z0}V_a^2 + \langle c_{z\alpha}(y), w(y)\rangle V_a. \tag{28}$$

Following the discussions in Section 2 and neglecting polynomial coefficients higher than 2, i.e., $w(y) = \zeta_0 p_0 + \zeta_1 p_1 + \zeta_2 p_2$, (28) can be evaluated to

$$a_z = c_{z0}V_a^2 + c_{z\zeta_0}\zeta_0 V_a + c_{z\zeta_2}\zeta_2 V, \tag{29}$$

With $c_{z\zeta_0} = \langle c_{z\alpha}(y), p_0(y)\rangle$, $c_{z\zeta_2} = \langle c_{z\alpha}(y), p_2(y)\rangle$, and $\langle c_{z\alpha}(y), p_1(y)\rangle = 0$ for symmetry reasons.
To calculate estimated values $\hat{\zeta}_0$ and $\hat{\zeta}_2$ of the coefficients ζ_0 and ζ_2, the vertical wind at the UAS probes $\boldsymbol{w}_{0,2} = [w_L \quad w_C \quad w_R]^T$ can be written as

$$\boldsymbol{w}_{0,2} = \boldsymbol{P}_{0,2}\boldsymbol{\zeta}_{0,2}, \tag{30}$$

with the matrix

$$\boldsymbol{P}_{0,2} = \begin{bmatrix} p_0(y_L) & p_1(y_L) & p_2(y_L) \\ p_0(y_C) & p_1(y_C) & p_2(y_C) \\ p_0(y_R) & p_1(y_R) & p_2(y_R) \end{bmatrix} = \begin{bmatrix} 1 & -1.05 & 0.12 \\ 1 & 0 & -1.12 \\ 1 & 1.05 & 0.12 \end{bmatrix}. \tag{31}$$

As $\boldsymbol{P}_{0,2}$ is a regular matrix, the estimated polynomial coefficients $\hat{\boldsymbol{\zeta}}_{0,2} = [\hat{\zeta}_0 \quad \hat{\zeta}_1 \quad \hat{\zeta}_2]^{\mathrm{T}}$ based on the three measurement $\boldsymbol{w}_{0,2}$ are determined as

$$\hat{\boldsymbol{\zeta}}_{0,2} = \boldsymbol{P}_{0,2}^{-1}\boldsymbol{w}_{0,2}. \tag{32}$$

Finally, based on these considerations, for the UAS testbed the predicted acceleration $\hat{a}_z$ with anticipation distance $d_{ant} = d_{x,CG} = \frac{b}{2} = 0.8$m is calculated as,

$$\hat{a}_z\left(t + \frac{d_{ant}}{V_a(t)}\right) = c_{z0}V_a(t)^2 + c_{z\zeta_0}\hat{\zeta}_0(t)V_a(t) + c_{z\zeta_2}\hat{\zeta}_2(t)V_a(t). \tag{33}$$

5. TEST FLIGHT DATA ANALYSIS

To investigate on the possibilities to predict the vertical acceleration of an aircraft in atmospheric turbulence by differential pressure measurements in front of the wings, test flights with a UAS testbed, c.f., Section 3, are performed. The flights are conducted in different intensities of atmospheric turbulence from moderate turbulence with g-load variations of a_z in the order of 0.5g up to severe turbulence with variations of the g-load of more than 3g, with the gravitational acceleration 1g=9.81m/s².

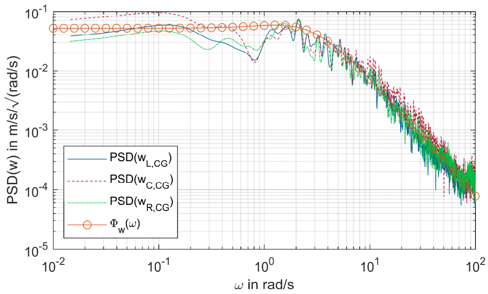

Figure 8: Comparison of the PSDs of $w_{L,CG}$, $w_{C,CG}$, $w_{R,CG}$ with the PSD $\Phi_w(\omega)$ of turbulence model (1), L_w = 3m.

First the spectral properties of the measured turbulence are assessed by comparing the PSD of the vertical wind measured with the three probes $w_{L,CG} = \alpha_{L,CG} V_a$, $w_{C,CG} = \alpha_{C,CG} V_a$, $w_{R,CG} = \alpha_{R,CG} V_a$ to the turbulence model (1) with the temporal PSD $\Phi_w(\omega)$, which is calculated making use of transformation (5). Figure 8 shows the result for L_w = 3m, σ_w = 0.6m/s² and V_a = 13.4m/s, where V_a and σ_w are the mean values of the measurements in flight and L_w is the fitted parameter. A very good compliance of the measured turbulence field with $\Phi_w(\omega)$ can be observed. The measurements of the three probes show similar PSD magnitudes. By the correction of turn rates (20) measurement errors due to the short period mode oscillation [21] are corrected, while the uncorrected phugoid mode with a time constant $T_{ph} \approx 8s$ seems to affect measurements in the region of $\omega_{ph} \approx \frac{2\pi}{8s} = 0.78\,\frac{rad}{s}$. To determine the parameters c_{z0}, $c_{z\zeta_0}$, $c_{z\zeta_2}$ of (33) a least squares optimization problem is solved to minimize the prediction error e_{a_z} of the recorded flight data. Additionally, it showed to be beneficial to also introduce a fourth parameter c_{zV_a} to account for linear effects of V_a, which lead to the predicted acceleration

$$\hat{a}_z = c_{z0} {V_a}^2 + c_{zV_a} V_a + c_{z\zeta_0} \zeta_0 V_a + c_{z\zeta_2} \zeta_2 V_a. \qquad (34)$$

The optimal parameters result as $c_{z0} = -0.017$, $c_{zV_a} = 0.565$, $c_{z\zeta_0} = 0.618$, and $c_{z\zeta_2} = 0.148$ based on the test flight data for different turbulence intensities.

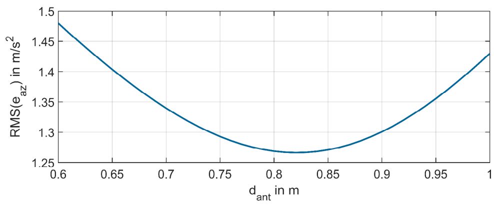

Figure 9: Analysis how the anticipation distance d_{ant} affects $RMS(e_{a_z})$ in the range of $d_{ant} = d_{x,CG} \pm 0.2$m.

As first consideration, before presenting time and frequency analysis of $\hat{a}_z$, the anticipation distance d_{ant} shall be validated by calculating $\hat{a}_z$ according to (34) with d_{ant} in the range $d_{x,CG} \pm 0.2\mathrm{m}$, i.e., from $0.6\mathrm{m}$ to $1\mathrm{m}$ for moderate turbulence. To this end, Figure 9 shows the RMS value of the prediction

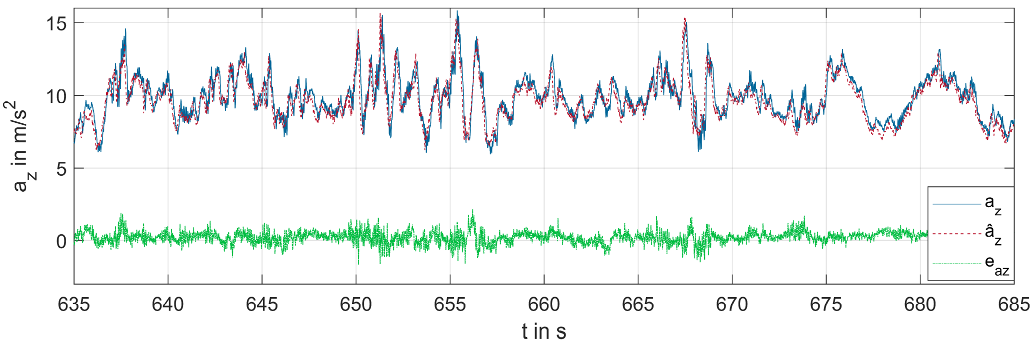

Figure 10: Acceleration a_z, predicted acceleration $\hat{a}_z$, and prediction error e_{a_z} for moderate turbulence.

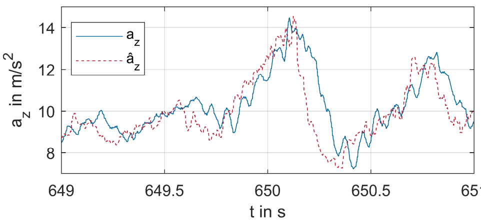

Figure 11: Detail view of Figure 10, where the predicted acceleration $\hat{a}_z$ appears shifted relatively to a_z by the anticipation time $T_{ant} \approx 0.1s$.

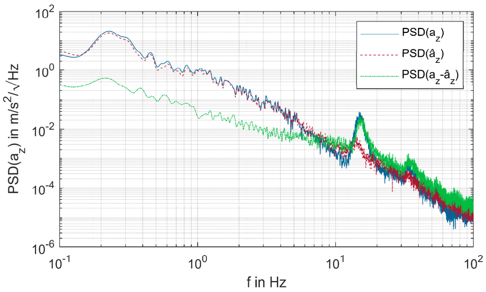

Figure 12: PSD of acceleration a_z, predicted acceleration $\hat{a}_z$, and prediction error e_{a_z} for moderate turbulence.

error e_{a_z}, which becomes minimal for $d_{ant} =$ 0.821m. As only a small deviation of 0.021m from $d_{x,CG} = 0.8$m is observed, which increases the RMS(e_{a_z}) by less than 1%, the geometry based anticipation distance $d_{ant} = d_{x,CG} = \frac{b}{2} = 0.8$m is kept for the following investigations. It shall be emphasized, that while d_{ant} is constant, according to (24) the anticipation time T_{ant} varies depending on the airspeed from 0.1s for low airspeeds $V_a =$ 8m/s to 0.05s for high airspeeds $V_a =$ 16m/s.

To assess the ability of $\hat{a}_z$ to predict the time behavior of a_z in moderate turbulence, Figure 10 presents the time signal of a_z, $\hat{a}_z$, and the prediction error e_{a_z}. An accurate prediction of the time behavior can be observed, where e_{a_z} for the most part stays below 1m/s², while a_z varies from 6m/s² up to 16m/s².

To allow for a more detailed examination of the predictive character of $\hat{a}_z$, Figure 11 shows a 2s time interval from 649s to 651s of Figure 10. The predicted acceleration $\hat{a}_z$ appears shifted by the anticipation time $T_{ant} \approx 0.1s$ relatively to a_z, which is consistent with the flown airspeed $V_a \approx$ 8m/s during this time interval.

To assess the frequency behavior, the PSD of a_z, $\hat{a}_z$, and e_{a_z} for moderate turbulence are presented in Figure 12. For frequencies below 2Hz the PSD of the prediction error PSD(e_{a_z}) is more than 10 times lower than PSD(a_z). Above 2Hz, PSD(e_{a_z}) is noticeably increasing relatively to PSD(a_z), up to reaching similar values at 8Hz. At 15Hz PSD(a_z) shows a pronounced peak, which probably is related to oscillations of the air data boom. The slightly higher slope of PSD(a_z) after the resonance can be an indication for a decoupling antiresonance, however, further investigations and design improvements are planned to investigate on this resonance phenomenon.

To assess the ability of $\hat{a}_z$ to predict the time behavior of a_z also in severe turbulence, Figure 10 presents the time signal of a_z, $\hat{a}_z$, and the prediction error e_{a_z}. A mostly accurate prediction of the time behavior can be observed, where e_{a_z} for the most part stays below 2m/s², while a_z varies from -1m/s² up to 35m/s². An error of over 5m/s² can be observed at 829s when the acceleration peak of 35m/s² is reached. As the high acceleration value correlates to high AOA α, the wings at this point most probably already show airflow detachment,

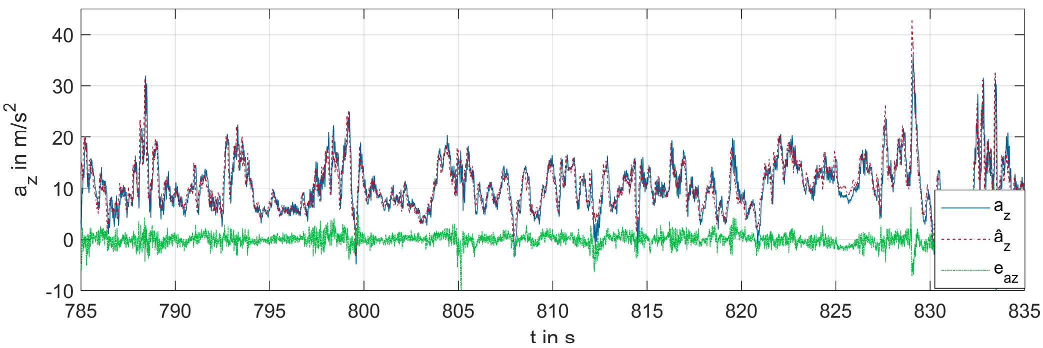

Figure 13: Acceleration a_z, predicted acceleration $\hat{a}_z$, and prediction error e_{a_z} for severe turbulence.

$\hat{\zeta}_0$=	$\alpha_L V_a$	$\alpha_C V_a$	$\alpha_{L,CG} V_a$	$\alpha_{C,CG} V_a$	$\alpha_{LR} V_a$	$(\hat{\zeta}_0)$	$(\hat{\zeta}_0, \hat{\zeta}_2)$
c_{z0}	0.012	0.024	-0.017	-0.002	-0.024	-0.022	-0.017
c_{zV_a}	0.311	0.163	0.709	0.467	0.640	0.614	0.565
$c_{z\zeta_0}$	0.663	0.544	0.499	0.494	0.654	0.644	0.618
$c_{z\zeta_2}$	0	0	0	0	0	0	-0.148
$RMS(e_{a_z})$, severe	3.095	2.674	2.359	1.736	1.503	1.444	1.389
$RMS(e_{a_z})$, moderate	1.469	1.247	0.908	0.783	0.698	0.674	0.651
ε_{a_z}, severe	27.23%	23.54%	20.76%	15.27%	13.23%	12.70%	12.22%
ε_{a_z}, moderate	14.33%	12.16%	8.86%	7.64%	6.81%	6.58%	6.35%

Table 2: Comparison of $RMS(e_{a_z})$ and relative error ε_{a_z} for different cases of $\hat{\zeta}_0$ for moderate and severe turbulence.

such that the lift model (25) would need to be extended by nonlinear terms of α for more accurate tracking of a_z.

The difference of flying in moderate turbulence and severe turbulence is additionally illustrated by Figure 14 and Figure 15, which show the empirical probabilities $\Pr(a_z)$ and $\Pr(e_{a_z})$ of a_z and e_{a_z} with a bin width of 0.2m/s². All empirical probabilities show distributions approximately according to Gaussian curves. For both turbulence intensities $\Pr(a_z)$ shows a mean value around 1g=9.81m/s². Regarding the variation, as can be expected, for severe turbulence the values of a_z vary more intensely leading to a broader distribution $\Pr(a_z)$. The distributions of $\Pr(e_{a_z})$ for both Figures show a mean value of approximately 0 and are much narrower than $\Pr(a_z)$, being indicative for a good tracking performance.

Finally, the impact of $\hat{\zeta}_0$ and $\hat{\zeta}_2$ as well as the use of different probe configurations to determine these values is assessed for moderate and severe turbulence. To this end, for seven different cases Table 2 states the RMS value $RMS(e_{a_z})$ as well as the relative error

$$\varepsilon_{a_z} = \frac{RMS(e_{a_z})}{RMS(a_z)} = \frac{RMS(a_z) - RMS(\hat{a}_z)}{RMS(a_z)}, \qquad (35)$$

being related to the reference value $RMS(a_z)$ =10.25m/s² for moderate turbulence and $RMS(a_z)$ =11.36m/s² for severe turbulence. The parameters c_{z0}, c_{zV_a}, $c_{z\zeta_0}$, and $c_{z\zeta_2}$ are calculated by least squares optimization for each case individually to obtain a fair comparison of the achievable prediction error e_{a_z} for each case.

For the first six cases $c_{z\zeta_2} = 0$, i.e. assuming only a 0-th order field $w_0(y) = \hat{\zeta}_0 p_0(y)$, c.f., Section 2, while for the last case also the estimated 2-nd order coefficient $\hat{\zeta}_2$ is included. The lowest prediction performance is obtained for $\hat{\zeta}_0 = \alpha_L V_a$ and $\hat{\zeta}_0 = \alpha_C V_a$, i.e., single measurements without turn rate compensations (20). The turn rate compensations included in $\hat{\zeta}_0 = \alpha_{L,CG} V_a$ and $\hat{\zeta}_0 = \alpha_{R,CG} V_a$ noticeably improve the prediction accuracy, e.g., for moderate turbulence from 14.33% to 8.86% for the left probe and 12.16% to 7.64% for the center probe. Comparing the result for the left probe with the center probe, it can be noted that the center probe shows better performance. That an off-center probe performs worse than the center probe may be explained, as for the off-center probe also odd order fields $\zeta_1, \zeta_3, \ldots$ are projected into $\hat{\zeta}_0$ increasing spatial aliasing effects and, additionally, torsional movements of the air data boom cause off-center errors only.

The case $\hat{\zeta}_0 = \alpha_{LR} V_a$ includes two measurements, namely of the left and the right probe with the mean AOA $\alpha_{LR} = 0.5\,(\alpha_{L,CG} + \alpha_{R,CG})$, where $RMS(e_{a_z})$ and ε_{a_z} are further reduced, e.g., to 6.81% for moderate turbulence. Finally, the cases $(\hat{\zeta}_0)$ and $(\hat{\zeta}_0, \hat{\zeta}_2)$

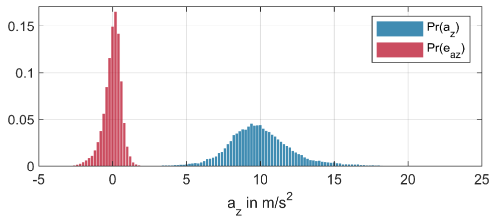

Figure 14: Empirical probability $Pr(a_z)$ and $Pr(e_{a_z})$ with bin width 0.2m/s² for moderate turbulence.

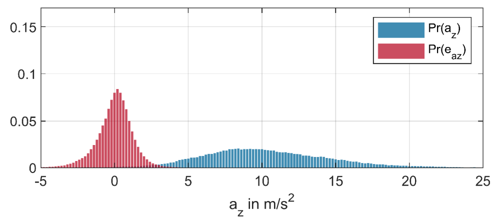

Figure 15: Empirical probability $Pr(a_z)$ and $Pr(e_{a_z})$ with bin width 0.2m/s² for severe turbulence.

include all three measurements according to (32), where $(\hat{\zeta}_0)$ only takes the 0-th order coefficient and $(\hat{\zeta}_0, \hat{\zeta}_2)$ also includes the 2-nd order coefficient, what becomes apparent by the non-zero parameter $c_{z\zeta_2}$. As expected, by taking all three measurements into account the prediction error is further reduced. Also including $\hat{\zeta}_2$ results in a slightly better performance, than for $\hat{\zeta}_0$ only, e.g., for moderate turbulence ε_{a_z} is reduced from 6.58% to 6.35%, i.e., a prediction accuracy of 93.65%.

To further improve the prediction accuracy, especially for higher disturbance frequencies, c.f., Figure 12, research on the following error sources may be conducted:

- the time change of the turbulence field itself, i.e., the turbulence field may not be able to be assumed frozen,
- spatial aliasing, as higher order coefficients ζ_3, ζ_4, … are neglected,
- measurement errors such as miscalibration, limited bandwidth and measurement noise,
- flight dynamics such as forces and moments due to turn rates and control surface actuation,
- transient aerodynamic effects as air flow disturbances travel over aerodynamic surfaces, such as downwash effects,
- structural modes of the air data boom and the aircraft itself.

In summary, by analyzing time, frequency, and statistical characteristics of the predicted acceleration $\hat{a}_z$, it can be concluded, that the use of anticipating high-dynamic differential pressure measurements is a very promising approach for turbulence prediction. The measured prediction accuracy of over 90% will allow to advantageously use the predicted acceleration $\hat{a}_z$ for feedforward disturbance rejection in future work, especially bearing in mind the anticipation time of up to 0.1s, which allows for data processing and compensation of limited actuator dynamics.

6. CONCLUSION AND OUTLOOK

In this paper the prediction of the vertical acceleration of an aircraft in atmospheric turbulence by means of high-dynamic differential pressure sensors has been investigated. A spatial and temporal turbulence model is presented to develop a turbulence prediction formulation which is validated by actual test flights with a UAS platform in moderate and severe turbulence. By determining the airflow in front of the wings, an anticipation time of the predicted acceleration of up to 0.1s is obtained, which can be used to compensate for time delays and low-pass behavior of actuators and control algorithms. The prediction accuracy is assessed to be 93.65% for moderate turbulence and 87.78% for severe turbulence, where vertical acceleration disturbances higher than 30m/s^2 are measured.

By deflecting control surfaces according to the predicted disturbances, a significant reduction of turbulence effects on the flight dynamics of an aircraft is expected in future work, which is aimed at improving energy efficiency, safety, and passenger comfort of manned aviation.

7. ACKNOWLEDGEMENT

This work is funded by the Austrian Federal Ministry for Transport, Innovation and Technology within the framework of the Austrian aviation program TAKE OFF, project 874461 – SmartWings.

8. REFERENCES

[1] Wayne L. Golding, “Turbulence and Its Impact on Commercial Aviation,” *Journal of Aviation/Aerospace Education & Research*, vol. 11, no. 2, p. 11, 2002.

[2] C. Amaral, C. S. Dickson, and B. Watts, “NASA Turbulence Technologies In-Service Evaluation : Delta Air Lines Report-Out,” 2007.

[3] R. Sharman and T. Lane, *Aviation turbulence: Processes, detection, prediction*. Springer, 2016.

[4] P. D. Williams, “Increased light, moderate, and severe clear-air turbulence in response to climate change,” *Advances in Atmospheric Sciences*, vol. 34, no. 5, pp. 576–586, 2017.

[5] C. D. Regan and C. V Jutte, “Survey of Applications of Active Control Technology for Gust Alleviation and New Challenges for Lighter-weight Aircraft,” 2012.

[6] N. Fezans, H.-D. Joos, and C. Deiler, “Gust load alleviation for a long-range aircraft with and without anticipation,” *CEAS Aeronautical Journal*, pp. 1–25, 2019.

[7] T. von Karman, “Progress in the Statistical Theory of Turbulence,” *Proceedings of the National Academy of Sciences*, 1948.

[8] H. L. Dryden, “A review of the statistical theory of turbulence,” *Quarterly of Applied Mathematics*, vol. 1, no. 1, pp. 7–42, 1943.

[9] N. P. Schmitt, W. Rehm, T. Pistner, P. Zeller, H. Diehl, and P. Navé, “The AWIATOR airborne LIDAR turbulence sensor,” *Aerospace Science and Technology*, vol. 11, no. 7–8, pp. 546–552, 2007.

[10] H. P. J. Veerman, P. Vrancken, and L. Lombard, “Flight testing delicat – A promise for medium-range clear air turbulence protection,” *European 46th SETP and 25th SFTE Symposium, 15-18 June 2014*, no. June, pp. 15–18, 2014.

[11] N. Fezans, J. Schwithal, and D. Fischenberg, “In-flight remote sensing and identification of gusts, turbulence, and wake vortices using a Doppler LIDAR,” *CEAS Aeronautical Journal*, vol. 8, no. 2, pp. 313–333, 2017.

[12] A. Mohamed, M. Abdulrahim, S. Watkins, and R. Clothier, “Development and Flight Testing of a Turbulence Mitigation System for Micro Air Vehicles,” *Journal of Field Robotics*, vol. 33, no. 5, pp. 639–660, 2016.

[13] A. Mohamed, S. Watkins, R. Clothier, and M. Abdulrahim, “Influence of turbulence on MAV roll perturbations,” *International Journal of Micro Air Vehicles*, vol. 6, no. 3, pp. 175–190, 2014.

[14] G. M. Gremillion, L. M. Castano, and J. S. Humbert, “Disturbance rejection with distributed acceleration and strain sensing,” *AIAA Guidance, Navigation, and Control Conference, 2013*, no. January, pp. 1–17, 2015.

[15] A. Galffy, M. Böck, and A. Kugi, “Nonlinear 3D path following control of a fixed-wing aircraft based on acceleration control,” *Control Engineering Practice*, vol. 86, pp. 56–69, May 2019.

[16] R. Sanz, P. Garcia, and P. Albertos, “Enhanced disturbance rejection for a predictor-based control of LTI systems with input delay,” *Automatica*, vol. 72, pp. 205–208, 2016.

[17] N. Fezans and H.-D. Joos, “Combined Feedback and LIDAR-Based Feedforward Active Load Alleviation,” in *AIAA Atmospheric Flight Mechanics Conference*, 2017, pp. 1–30.

[18] M. Abdulrahim, “Control Strategies for Flight in Extreme Turbulence,” in *AIAA Guidance, Navigation, and Control Conference*, 2017.

[19] G. I. Taylor, “The Spectrum of Turbulence,” *Proceedings of the Royal Society of London. Series A - Mathematical and Physical Sciences*, 1938.

[20] A. Galffy, F. Car, and G. Schitter, “Calibration and flight test of a 3D printed 5-hole probe for high-dynamic wind measurements for UAV.”

[21] R. F. Stengel, *Flight dynamics*. Princeton University Press, 2004.